Journal of Industrial and Engineering Chemistry 109 (2022) 347–358

Contents lists available at ScienceDirect

Journal of Industrial and Engineering Chemistry

journal homepage: www.elsevier.com/locate/jiec

Phenol removal and hydrogen production from water: Silver nanoparticles decorated on polyaniline wrapped zinc oxide nanorods

Asim Jilani [a,*], Mohammad Omaish Ansari [a,*], Ghani ur Rehman [b], Muhammad Bilal Shakoor [c], Syed Zajif Hussain [d], Mohd Hafiz Dzarfan Othman [b], Sajid Rashid Ahmad [c], Mohsin Raza Dustgeer [e], Ahmed Alshahrie [a]

[a] Center of Nanotechnology, King Abdulaziz University, 21589 Jeddah, Saudi Arabia
[b] Advanced Membrane Technology Research Centre, Universiti Teknologi Malaysia, 81310 UTM Johor Bahru, Johor, Malaysia
[c] College of Earth and Environmental Sciences, University of the Punjab, Lahore 54000, Pakistan
[d] Department of Chemistry & Chemical Engineering, SBA-School of Science & Engineering (SBA-SSE), Lahore University of Management Sciences (LUMS), Lahore 54792, Pakistan
[e] Department of Environmental Sciences and Engineering, Government College University Faisalabad, Faisalabad, Pakistan

ARTICLE INFO

Article history:
Received 17 November 2021
Revised 2 January 2022
Accepted 8 February 2022
Available online 14 February 2022

Keywords:
Ternary polymer photocatalyst
Hydrogen production
Phenol degradation
Response surface methodology

ABSTRACT

The toxic and carcinogenic organic compounds discharge from industries, contaminate the natural reservoirs of water and air which eventually pose a global threat not only to the aquatic life but also to the humanity. Herein, ternary nanocomposites of silver-nanoparticle (AgNPs)-decorated on polyaniline (Pani)-wrapped zinc oxide nanorods (AgNPs@Pani/ZnO) were prepared via a facile approach. The nanocomposite degraded 97.91% phenol with an optimized dosage and concentration of H_2O_2. Moreover, the apparent rate constant for phenol degradation was 3.69 times higher than for pure ZnO nanorods. The hydrogen production from AgNPs@Pani/ZnO was 1.58 and 2.74 times higher than Pani/ZnO and ZnO, respectively. The enhanced phenol degradation and hydrogen production is attributed to the transfer of holes to the Pani, from which the electrons were transferred to the conduction band of ZnO and eventually to the conduction band of the AgNPs, where they accelerated the redox reactions for rapid photolysis of water and phenol. The concentration of the catalyst dosage affected the rate of phenol degradation. Further, response surface methodology was also applied in order to design 13 sets of random experiments in which the catalyst dosage and degradation time were varied to predict the phenol degradation.

Introduction

Photocatalytic degradation of pollutants with simultaneous hydrogen production is one of the greener processes aimed to solve the environment remediation issues and energy crisis [1–3]. The process is economical and simpler in contrast to photocatalytic water splitting reaction for hydrogen generation or electrocatalytic hydrogen production as these require costly instruments and involves tedious techniques [4,5]. Wastewater discharge from the chemical industry contains a substantial concentration of highly toxic and refractory organic pollutants. Thermochemical processes using wood-based by-products add significant phenolic compounds (such as 2-chlorophenol, o-cresol, and p-nitrophenol) to water, ranging from 500 to 1000 mg L^{-1} [6–8]. Phenols have been extensively used as monomers for polycarbonate production and epoxy resins in various plastic manufacturing processes [9,10]. In general, phenol concentrations of 9 to –25 mg L^{-1} are considered harmful to aquatic organisms and humans [7]. Owing to their unique physicochemical properties and complex structure, phenolic compounds may disturb endocrine systems and restrict or block the normal functioning of natural hormones [11,12]. Thus, the United States Environment Protection Agency (US-EPA) has set the maximum allowable level of phenol contamination as <2 mg L^{-1} in drinking water and <1 μg L^{-1} in surface water [7,13]. Due to the potential toxicity of phenols and their effects on human health, it is necessary to develop cost-effective and efficient remediation technologies to remove phenols from wastewater [14,15].

Several conventional techniques, including distillation, oxidation, and solvent extraction, have been used to remove phenolic compounds from water. However, these techniques have proven

* Corresponding authors.
E-mail addresses: ajilani@kau.edu.sa, asim.jilane@gmail.com (A. Jilani), omaish-chem@gmail.com (M.O. Ansari).

https://doi.org/10.1016/j.jiec.2022.02.021
1226-086X/

costly, inefficient, non-user-friendly, and inapplicable at commercial scales [9,15]. Photocatalytic degradation has emerged as a promising method for removing phenolic compounds without any major drawbacks compared to these conventional methods. Moreover, these photocatalysts can degrade other organic compounds and are easy to synthesize and handle [16].

The desirable properties in such photocatalysts are a small bandgap, appropriate surface morphology, high surface area, stability, and reusability. These properties result in highly efficient activity. Pure metal oxides, such as titanium dioxide, cadmium oxide, and vanadium pentoxide, have been widely used as pioneer photocatalytic materials. However, the large bandgap of >3 eV limits their usage in the visible light region, and thus bandgap engineering is required for their usage under a wide spectral range. Polyaniline (Pani) has been used to attain superior absorption in the UV and visible light regions for metal oxides, owing to its small bandgap of ~2.8 eV. Pani can supply electrons and holes (donor–acceptor) for the photosensitizer [17]. The lowering of the bandgap by Pani is due to the π-π^* transition on irradiation: the excited electrons are transferred to the π^* orbital and can be readily transferred to the conduction band of metal oxides [18]. Pani also decreases the charge recombination ratio, affects the concentration of hydroxyl free radicals, and shifts the photo-response of metal oxides to the visible light regions [16].

Among different metal oxides, zinc oxide (ZnO) has numerous advantages, including ease of synthesis, low cost, high stability, tunable bandgap, and an eco-friendly nature [19,20]. The comparative table (Supplementary Table S1) revealed the potential use of ZnO and its composites with metal/oxides and polymers to degrade the various harmful pollutants from water. In combination with ZnO, Pani is expected to show a reduced bandgap and high absorption under a wide range of solar radiation. The performance of Pani/ZnO can be further improved by the incorporation of Ag [21]. Introducing Ag resulted in enhanced conductivity of Pani/ZnO because of the synergistic effect and increased light-harvesting ability owing to surface plasmon resonance (SPR) [22]. Furthermore, the high oxidation ability of Ag for organic pollutants under UV and visible light makes it an excellent dopant in the preparation of ternary photocatalytic materials [23].

Therefore, it is believed that ternary composites of ZnO, Pani, and Ag will prove to be efficient photocatalysts and have good light absorption properties due to the synergistic effect of ZnO, Pani, and Ag nanoparticles. In this work, silver nanoparticles impregnated on surface of Pani wrapped ZnO (AgNPs@Pani/ZnO) were prepared by the combustion of zinc acetate to prepare ZnO nanorods and later coating of Pani on it followed by subsequent deposition of Ag. The ternary composite possessed narrow bandgap, which reduced the charge recombination rate and enhanced the photocatalytic efficiency. The prepared nanocomposite, AgNPs@Pani/ZnO, was used to degrade phenol and produce hydrogen under visible light, and the obtained results were further validated by simulated response surface methodology (RSM) studies. The RSM aided understanding of the experimental and theoretical results that can be further validated by the analysis of variance (ANOVA).

Experimental section

Materials

Aniline, zinc acetate ($Zn(CH_3CO_2)_2$, silver nitrate ($AgNO_3$), N-methyl-2-pyrrolidone (NMP), oxidant-potassium persulfate (PPs), ascorbic acid, hydrochloric acid (HCl), ethanol, and ammonium hydroxide (NH_4OH) were purchased from Sigma Aldrich. Double distilled aniline was used for the Pani synthesis.

Material syntheses

The fabrication of AgNPs@Pani/ZnO was done by synthesizing ZnO nanorods and Pani and further their composite was decorated with AgNPs. Firstly, ZnO nanorods was prepared by the combustion of $Zn(CH_3CO_2)_2$ and for it 4.8 g of $Zn(CH_3CO_2)_2$ was added to 80 mL of ethanol to obtain a 60 mg mL^{-1} solution, which was sonicated and subjected to vigorous stirring until homogenous. The solution was subsequently left to settle until the $Zn(CH_3CO_2)_2$ recrystallized. The recrystallized $Zn(CH_3CO_2)_2$was collected by discarding the ethanol and subsequently heated in glass tube at 450 °C for 45 min to obtain ZnO nanorods [24,25].

Pani emeraldine base solution was prepared by in-situ oxidative polymerization of aniline. Firstly, 1 g of aniline was added to 100 mL of 1 M HCl solution and stirred, and in another beaker, the oxidant solution was prepared by dissolving 1.48 g of potassium persulphate in 100 mL of 1 M HCl. To polymerize the aniline, the oxidant solution was slowly added to the aniline dispersion. The color of the solution immediately changed to green, followed by a bluish-black color, thereby confirming the formation of Pani. The whole solution of Pani was left for 24 h for complete polymerization. The Pani was separated by filtration and centrifugation, further washed with excess of water and ethanol, and subsequently de-doped with 1 M ammonia solution to obtain Pani base. The Pani base was washed with excess water and ethanol and dried at 80 °C for 12 h. To prepare the Pani solution, 0.5 g of emeraldine base was dissolved in 50 mL of N-methyl-2-pyrrolidone and stirred. The undissolved Pani was removed by filtration and centrifugation, resulting in a homogenous Pani solution [25].

To coat the ZnO nanorods with Pani, 0.2 g of nanorods were spread on filter paper, and 0.2 mL of Pani solution was added to it dropwise. The filter paper absorbed the excess Pani, and after drying, the Pani-coated ZnO was removed, placed in a Petri dish and dried at 80 °C for 12 h to obtain Pani/ZnO.

To prepare the ternary AgNPs@Pani/ZnO nanocomposite, 0.5 g of Pani/ZnO was added to 100 mL of 0.002 M ascorbic acid, placed in an ice bath, and stirred for one hour. Next, 30 mL of 0.001 M $AgNO_3$ was added to the mixture of Pani/ZnO from a burette at the rate of one drop/second. The color of the mixture changed to gray, and the mixture was filtered and centrifuged to extract the AgNPs@Pani/ZnO. The AgNPs@Pani/ZnO was subsequently washed with water and ethanol followed by drying at 80 °C for 24 h. The schematic representation of the experimental procedure is shown in Fig. 1.

Characterizations

Structural properties of AgNPs@Pani/ZnO were evaluated through X-ray diffraction (XRD) spectroscopy of Rigaku (Ultima IV). The diffraction angle were fixed 5^O to 80^O for all prepared samples. Surface chemical composition was explored by X-ray photoelectron spectroscopy (XPS-Physical electronics VersaProbII) under high vacuum of $1.1x10^{-6}$ Pascal. The charge recombination ratio was investigated by photoluminescence spectroscopy (PL) of shimadzu-RF-5301PC while diffuse reflectance spectroscopy (HACH LANGE DR 6000) was used to calculate the optical band gap. Field emission scanning electron microscopy (FESEM) of JEOL (JSM7600 F) and transmission electron microscopy (TEM) was applied for the surface morphology of AgNPs@Pani/ZnO. The energy-dispersive X-ray spectroscopy (Oxford instrument –X-stream2) attached to JEOL (JSM7600 F) was also used to detect the elemental composition of AgNPs@Pani/ZnO.

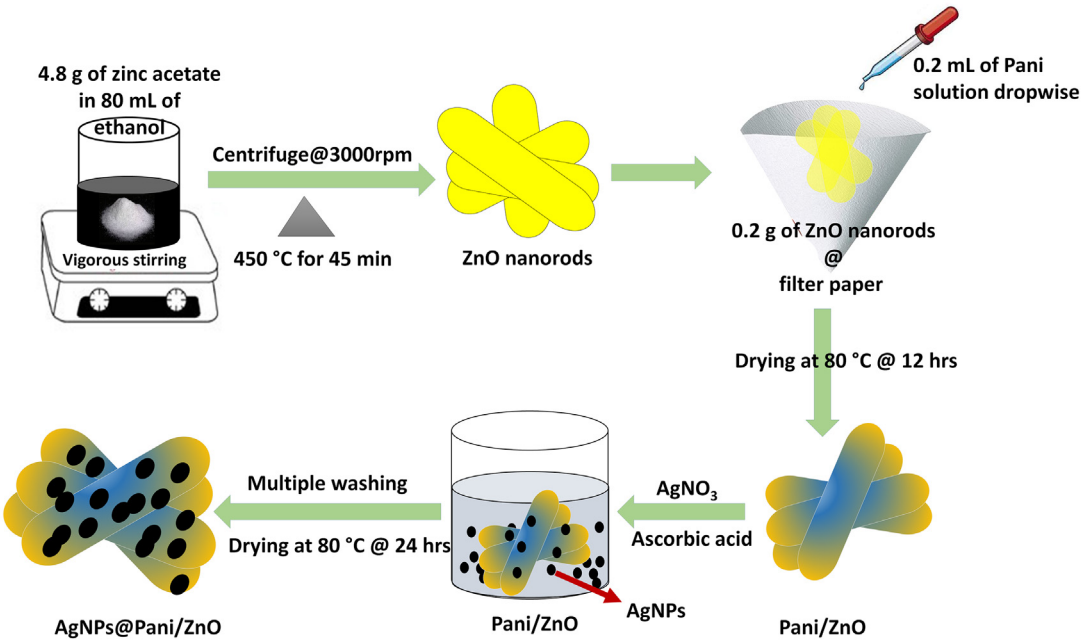

Fig. 1. Schematic illustration of the synthesis of AgNPs@Pani/ZnO.

Photocatalysis hydrogen production experiments

The photocatalytic activity of ZnO, Pani/ZnO, and AgNPs@Pani/ZnO was investigated by studying the degradation of phenol. In this experiment, 230 mg (optimized against 200 mg, 230 and 260 mg as presented in supplementary Fig. S1) of the photocatalyst was added to 350 mL of simulated wastewater containing 50 ppm phenolic contamination. To reach adsorption–desorption equilibrium, the solution was kept in the dark for 60 min. The phenol and catalyst mixture was irradiated by visible light (80 watt, 450 nm). Furthermore, a 10 mL aliquot of the solution was taken after an interval of 1 h, and the degradation of phenol was analyzed using UV–Visible spectroscopy. The degradation efficiency of ZnO, Pani/ZnO, and AgNPs@Pani/ZnO was calculated with the following equation [26]:

$$Degradation(\%) = (\frac{C_o - C_t}{C_o})100 \quad (1)$$

where C_o is the initial concentration of phenol, and C_t represents the phenol concentration after the set interval of time (1 h). After calculating the photocatalytic efficiency, the following equation was applied to find the apparent rate constant (k) for ZnO, Pani/ZnO, and AgNPs@Pani/ZnO [27].

$$\ln(\frac{C}{C_o}) = -kt \quad (2)$$

The hydrogen evolution reaction was performed using methanol (15%) as sacrificial agent with an optimized mass concentration of (0.4 g) AgNPs@Pani/ZnO.

Results and discussion

Structural analysis

The well-defined and sharp diffraction spectra (Fig. 2a) of ZnO, Pani/ZnO, and AgNPs@Pani/ZnO indicate that all prepared samples have a crystalline nature. The most intense diffraction plane observed was (101) at 2θ = 36.45, and all the observed diffraction planes (Supplementary Table S2) well matched with JCPDS# 01-078-3325, zinc oxide. However, after incorporating Pani onto ZnO (Fig. 2a), the diffraction peaks showed slight shifting in 2θ values owing to the interactions between the two, which is consistent with the previous literature [28]. Moreover, the diffraction peak of Pani is not distinct, and this can be attributed to the interaction of the hydrogen bonds of Pani and the oxygen vacancies of ZnO, and also to the low concent of Pani in the composite [29]. Further, additional diffraction peaks were observed for AgNPs@Pani/ZnO at 2θ = 38.25, 44.42, and 64.55, associated to the (111), (200), and (220) diffraction planes, respectively. These additional planes matched well with JCPDS # 00-001-1167, Ag. In summary, no unknown diffraction peaks were observed in ZnO, Pani/ZnO, or AgNPs@Pani/ZnO, indicating the efficacy of the synthesis methodology.

The addition of Pani and Ag to ZnO may change its grain size, thereby affecting the photocatalytic activity. Therefore, the grain size was calculated by applying the Scherrer equation [26]. The grain sizes (Fig. 2b) of ZnO, Pani/ZnO, and AgNPs@Pani/ZnO were calculated to be 30.68, 26.58, and 29.97 nm, respectively. The decrease in the grain size of Pani/ZnO in comparison to pure ZnO is attributed to the strong interaction and hitching of Pani molecules to the surface of ZnO [30,31]. Moreover, in AgNPs@Pani/ZnO, a smaller reduction in grain size was noticed compared to pure ZnO. This variation is due to the difference in the ionic radii of ZnO (0.74 Å) and Ag (1.26 Å) [32]. The reduction in grain size after adding Ag is also in good agreement with previous studies [33].

Chemical state analysis

The surface of the photocatalyst provides attractive sites to capture the pollutants from the wastewater; therefore, XPS was used to analyze the surface composition of ZnO, Pani/ZnO, and AgNPs@Pani/ZnO. Fig. 3a shows the survey scan, while Fig. 3b gives the atomic weight percentage of each detected element. A survey scan of ZnO shows only Zn and O1s, while the scan of Pani/ZnO revealed additional C1s and N1s peaks. These additional peaks con-

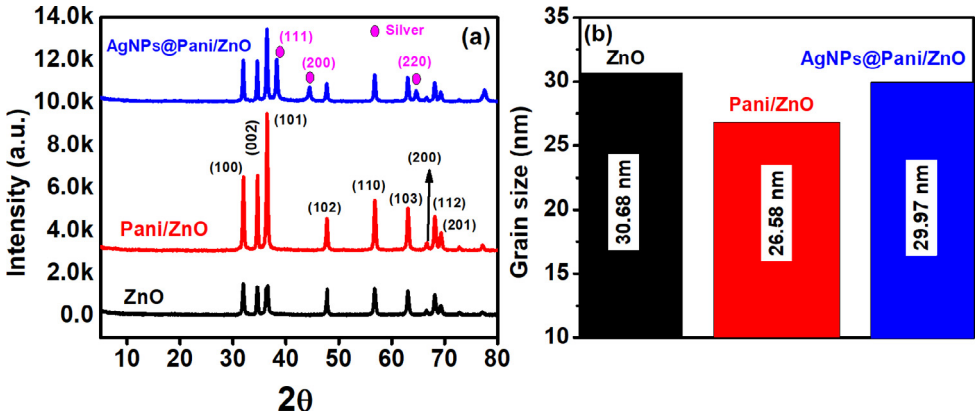

Fig. 2. (a) Diffraction spectra and (b) calculated grain sizes of ZnO, Pani/ZnO, and AgNPs@Pani/ZnO.

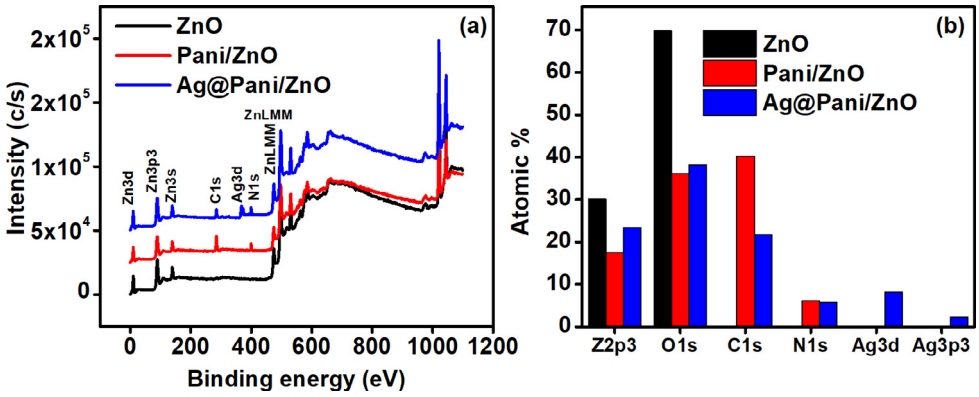

Fig. 3. (a) Survey scan and (b) detected atomic percentages of elements in ZnO, Pani/ZnO and AgNPs@Pani/ZnO.

firm the presence of Pani alongside ZnO. Furthermore, in the case of AgNPs@Pani/ZnO, the presence of Ag3d and Ag3p3 peaks supports the addition of Ag to Pani/ZnO. Moreover, the absence of any other unknown peak for ZnO, Pani/ZnO, or AgNPs@Pani/ZnO substantiates the efficacy of the synthesis technique. The atomic percentages of Zn2p for ZnO, Pani/ZnO, and AgNPs@Pani/ZnO were 30.1, 17.5, and 23.5%, respectively, while the percentage of O1s was 69.9, 36.1, and 38.3%, respectively (Fig. 3b). The amount of C1s present in Pani/ZnO and AgNPs@Pani/ZnO was 40.3 and 21.8%, respectively. In AgNPs@Pani/ZnO, the Ag3d and Ag3p3 peaks were detected at percentages around 8.3 and 2.3%, respectively. Moreover, the N1s peak was around 6.1 and 5.8% for Pani/ZnO and AgNPs@Pani/ZnO, respectively.

The XPS study was extended to investigate the functional groups attached to the detected elements. Therefore, chemical state analysis of Zn2p3, Ag3d, C1s, N1s, and O1s was performed. The Zn2p3 of ZnO (Fig. 4a) shows two peaks at 1021.09 and 1022.58 eV with a separation of 1.48 eV. These peaks are attributed to metallic Zn and also Zn with oxygen vacancies (Zn-O) [34]. However, when Pani and Ag were added to ZnO (Fig. 4b and 4c), the separation between Zn and Zn-O changed to 0.95 eV and 0.32 eV, respectively, confirming the successful interaction between ZnO, Pani, and Ag. Furthermore, the oxygen vacancies interaction (i.e., Zn-O) constantly increased from 8.51, to 20.33, and 79.77% for ZnO, Pani/ZnO, and AgNPs@Pani/ZnO, respectively. This increase in oxygen vacancy interactions provides sites for the capturing of the phenol molecules by reducing the charge recombination ratio, thereby resulting in the enhanced photocatalytic degradation of ZnO composites [35]. Moreover, the chemical state of Ag3d for AgNPs@Pani/ZnO (Fig. 4d) shows the appearance of $Ag3d_{5/2}$ and $Ag3d_{3/2}$ at 368 and 374 eV, respectively [34].

C1s spectra of Pani/ZnO (Fig. 5a) reveal the existence of aliphatic carbon (C–C), carboxyl (C–O), and carboxylate (O–C=O) functional groups with atomic percentages of 68.96, 24.32, and 6.72, respectively. The peaks of these functional groups are located at 284.5, 285.5, and 288.4 eV, which is in agreement with previous studies of C1s [34]. However, with the addition of Ag to Pani/ZnO (Fig. 5b), the atomic percentages of functional groups changed to 29.83, 65.74, and 4.43% for C–C, C–O, and O–C=O, respectively. Moreover, an increase in hydroxyl functional groups also accelerates the photocatalytic process [36], which was also observed in our photocatalytic results (Fig. 9).

The N1s spectra of Pani/ZnO (Fig. 5c) and AgNPs/Pani/ZnO (Fig. 5d) revealed three peaks at 398.2, 399.8, and 401.5 eV, which is attributed to C–N bonds, O=C–N, and positively charged nitrogen ions ($-N^+$) [34,37]. However, the addition of Ag to Pani/ZnO affected the atomic percentages of these functional groups. The percentage of C-N was observed to be 49.87 and 17.01% for Pani/ZnO and AgNPs@Pani/ZnO, respectively. Furthermore, the percentage of O=C–N increased from 31.10 to 63.69% from Pani/ZnO to AgNPs@Pani/ZnO. Moreover, the difference in the percentage of $-N^+$ was 19.06 and 19.31% for Pani/ZnO and AgNPs@Pani/ZnO, respectively (Fig. 10).

The O1s spectra of ZnO (Fig. 6a) contained two peaks at 529.9 eV and 531.4 eV, which were attributed to the lattice oxygen (O_{lat}) and the hydroxyl group (–OH). The atomic percentage of O_{lat} and –OH was 62.54 and 37.46%, respectively [34]. However, with the addition of Pani and Ag (Fig. 6b–c), an additional peak was observed at 533.1 eV, which represented the attachment of oxygen

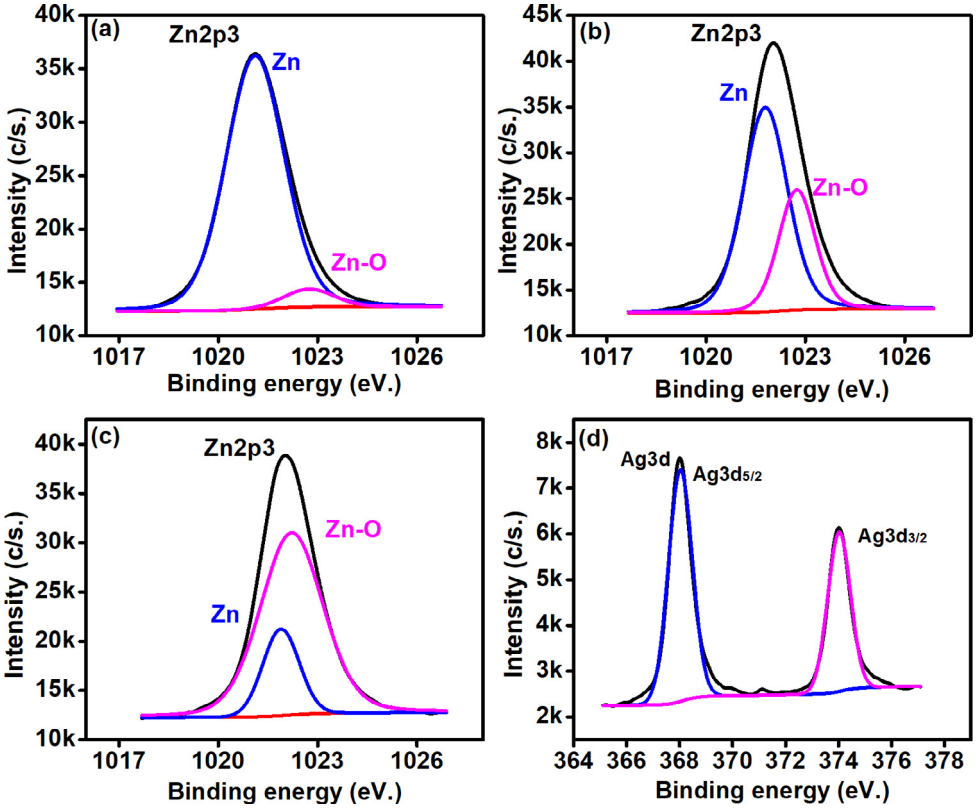

Fig. 4. Zn2p3 analysis of (a) ZnO, (b) Pani/ZnO, (c) AgNPs@Pani/ZnO and (d) Ag3d of AgNPs@Pani/ZnO.

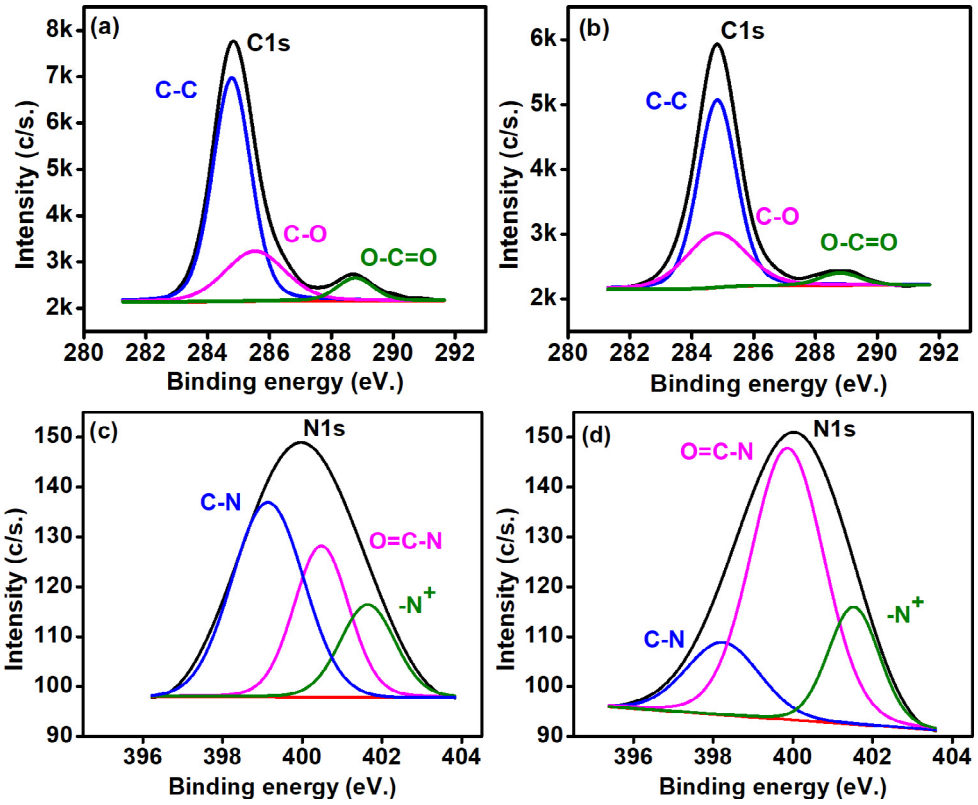

Fig. 5. C1s spectra of (a) Pani/ZnO and (b) AgNPs@Pani/ZnO and N1s spectra of (c) Pani/ZnO and (d) AgNPs@Pani/ZnO.

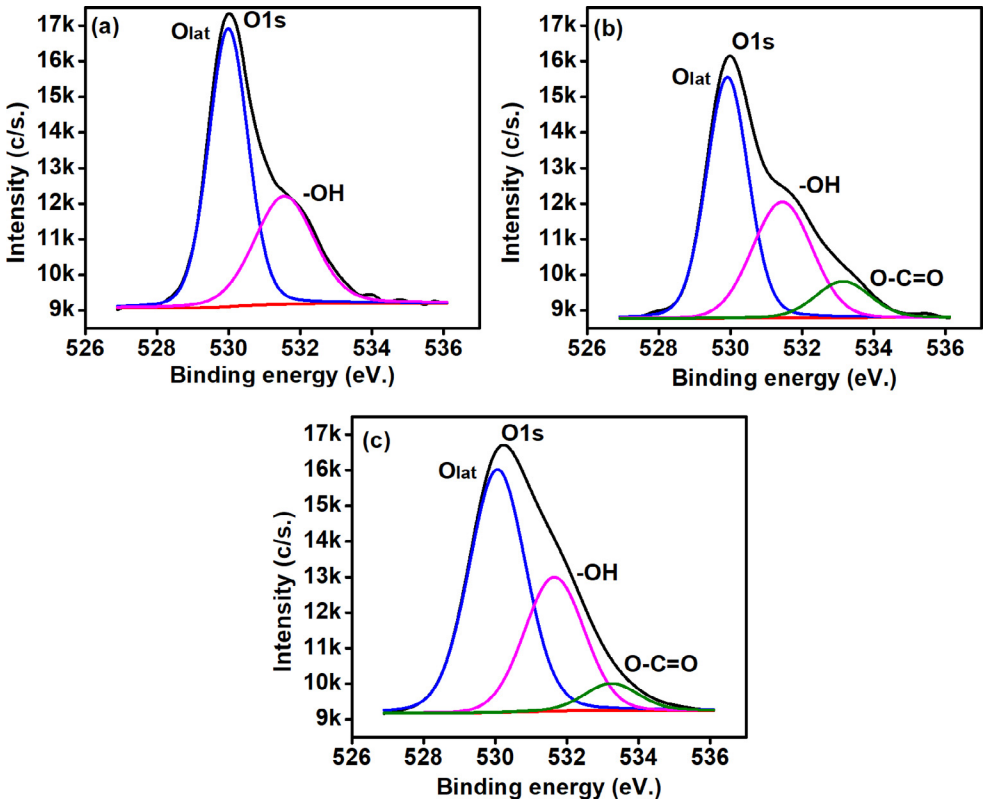

Fig. 6. O1s functional group evaluation for (a) ZnO, (b) Pani/ZnO, and (c) AgNPs@Pani/ZnO.

and carbon through single and double bonds (O–C=O) [34]. Therefore, Pani/ZnO and AgNPs@Pani/ZnO consisted of 10.40 and 6.37 %, respectively of O–C=O.

Optical properties

Fig. 7a shows the absorbance spectra of ZnO, Pani/ZnO, and AgNPs@Pani/ZnO. ZnO shows absorbance edge at around 400 nm, while in Pani/ZnO, this edge shifted to a higher wavelength, confirming the absorption of a higher number of photons [36]. Moreover, a small hump was observed in Pani/ZnO near 450 nm, which is attributed to the polaronic transition (π^*) of the Pani chain [38]. For AgNPs@Pani/ZnO, the absorption edge increased, and a small hump was noted at ~440 nm wavelength, attributed to the SPR of Ag. Moreover, SPR is a fundamental characteristic of Ag, attributed to the oscillation or absorption of light photons possessing higher energy levels. These properties could improve the charge carrier activity in AgNPs@Pani/ZnO, resulting in enhanced wastewater cleaning through a facile photocatalytic process.

Moreover, this charge movement affects the bandgap of the prepared photocatalyst computed using the following equation [39].

$$F(Reflectance(R)) = \left(\frac{1-R}{100}\right)^2 / 2R \quad (3)$$

The bandgap of ZnO (Fig. 7b) was calculated to be ~3.24 eV, which is lower than previously reported values [40]. The lower bandgap of the photocatalyst is due to its high conductivity. Furthermore, the bandgaps of Pani/ZnO and AgNPs@Pani/ZnO were observed to be ~3.21 and 3.13 eV, respectively (Fig. 7c), indicating the highly conductive nature of AgNPs@Pani/ZnO compared to the other two photocatalysts. The decrease in the bandgap from 3.24 eV to 3.13 eV showed the role of Pani and Ag in improving the shift of charge carriers from the valance shell to the conduction band of the prepared ternary AgNPs@Pani/ZnO.

The transferred charge carriers could recombine, affecting the photocatalytic performance of the prepared ternary nanocomposites. Moreover, higher charge recombination could result in lower photocatalytic performance of the nanomaterial for wastewater cleaning. Hence, the charge recombination ratios of the nanoparticles were demonstrated by PL spectra (Fig. 7d). For ZnO, the PL bands at ~392 and 468 nm were assigned to blue and green emissions, respectively [41,42]. The blue emission in the PL spectra shows the recombination of excitons from the conduction band to the valance band. In contrast, the green emission reflects surface defects due to Zn, interstitial O, and vacancies [43].

Furthermore, the PL spectral intensity is directly related to the charge recombination ratio. Here, the reduction in PL spectra intensity from the incorporation of Pani and Ag nanoparticles in ZnO supports a decrease in the charge recombination ratio of the photocatalyst. The shift in PL bands for Pani/ZnO compared to pure ZnO is due to the substantial reaction between the imine functional groups of Pani and the ZnO interstitials. This reaction could result in surface defects, which could offer attractive binding sites to remove contaminants. Moreover, AgNPs@Pani/ZnO had a broader PL spectra peak, which might be due to fluctuations in surface defects [44]. Overall, these surface defects, which indicate attractive sites, could increase the photocatalytic performance of the nanoparticles prepared for wastewater cleaning.

Surface morphology

The FSEM images of ZnO, Pani/ZnO, and AgNPs@Pani/ZnO are presented in Fig. 8a-c. In the case of pure ZnO (Fig. 8a), hexagonal rods with well-defined edges were observed. The length of the rods varies from ~100 to ~800 nm, while the thickness is <100 nm. The presence of several small rods may be due to the breakage of larger

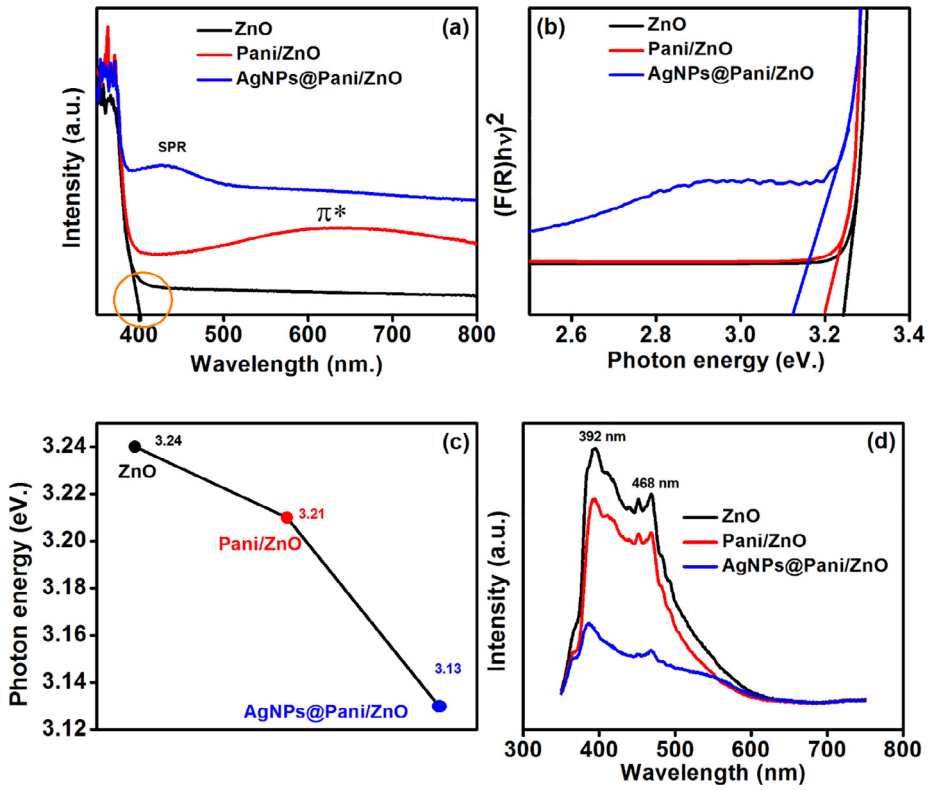

Fig. 7. (a) Absorption spectra, (b) bandgap conduction, (c) energy gap presentation, and (d) charge recombination ratio of ZnO, Pani/ZnO, and AgNPs@Pani/ZnO.

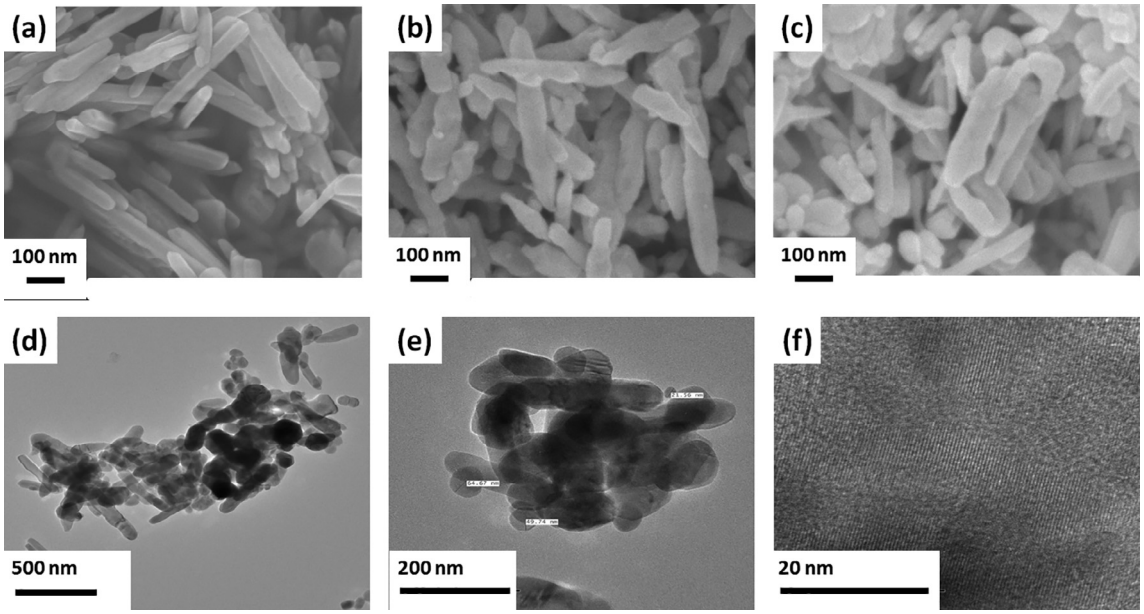

Fig. 8. FESEM analysis of ZnO (a), Pani/ZnO (b) and AgNPs@Pani/ZnO (c). TEM analysis of AgNPs@Pani/ZnO at different magnifications (d–f).

rods or due to seeds that failed to grow unidirectionally, resulting in breakage. Pani/ZnO (Fig. 8b) also shows rod-like morphology, but here the edges are broken and not well defined, which might be due to the penetration of Pani inside or the breakage or solubilization of ZnO during the coating process. The morphology of AgNPs@Pani/ZnO (Fig. 8c) is similar to Pani/ZnO, but small round Ag particles are present between the tubes at various places, suggesting the incorporation of Ag into Pani/ZnO. Many more Ag particles may be sandwiched or embedded inside and are not visible. Therefore, TEM analysis of AgNPs@Pani/ZnO was performed. Moreover, the energy dispersive spectroscopy was also used to investigate the elemental composition of prepared composites and the results (supplementary Fig. S2) showed the presence of zinc, oxygen, carbon nitrogen, and silver nanoparticles without any impuri-

ties. Moreover, elemental mapping of AgNPs@Pani/ZnO (supplementary Fig. S3) was also performed to reveal the distribution of detected elements.

The TEM images of AgNPs@Pani/ZnO show Ag nanoparticles anchored on Pani-coated ZnO (Fig. 8d–f). The observed thickness of the Pani-coated ZnO nanorods is ~60 nm, while the length is ~ 200 nm, and the observed diameter of the Ag nanoparticles is 20–60 nm.

Photocatalytic degradation of phenol

Photodegradation of phenol by AgNPs/Pani@ZnO

The performance of ZnO, Pani/ZnO, and AgNPs@Pani/ZnO for phenol degradation was investigated under visible light. However, before starting the photocatalytic experiments, 230 mg/350 mL photocatalyst was constantly stirred for 1 h in the dark to obtain adsorption–desorption equilibrium between the phenolic compound and the catalyst (Fig. 9a).

The photocatalytic activity of the ZnO (Fig. 9a) toward phenol was 31.61%. This low phenol degradation is due to the wide bandgap of the rapid recombination of charge carrier movements from the valence to the conduction band. However, after covering the ZnO with the Pani, phenol degradation was enhanced to 43.45%. The degradation by the Pani/ZnO was ~1.37 times higher than that of ZnO under the same experimental conditions. These results showed that the presence of Pani increased the activity of the ZnO. Subsequently, wrapping the ZnO with Pani chains allowed the excitation of the valence bond electrons of the photocatalyst under visible irradiation, which produces active radicals to degrade the phenolic compounds. Moreover, the insertion of Pani into ZnO nanorods could produce effective charge separation of electron and hole pairs, hindering rapid recombination of charge carriers, which can also be seen in the PL spectra (Fig. 7d).

The degradation of phenol was further accelerated by adding Ag nanoparticles to the Pani/ZnO. The AgNPs@Pani/ZnO photodegraded henol by 74.43%, which is greater than pure ZnO or Pani/ZnO. The enhancement of phenol degradation by AgNPs@Pani/ZnO is attributed to the formation of binary and ternary heterojunctions among ZnO, Pani, and Ag. Moreover, the SPR of Ag also contributes in enhancing the charge carrier movements by reducing the charge recombination ratio. These results are also consistent with the bandgap and PL analysis (Fig. 7b and d). The apparent rate constant of AgNPs@Pani/ZnO was 0.17202 which is, 1.53 and 3.69 times higher than Pani/ZnO and ZnO, respectively.

Role of environmental features

Influence of added H_2O_2 concentration on phenol photodegradation. The effects of adding H_2O_2 on phenol degradation were tested. The addition of H_2O_2 could produce greater OH^- concentrations, which can enhance the mineralization of pollutants. Therefore, ZnO, Pani/ZnO, and AgNPs@Pani/ZnO were tested using H_2O_2 (25 mM/H_2O_2 30% concentration), and the results are shown in Fig. 9d. The photocatalytic efficiency of the ZnO increased from 31.61 to 90.33%. This increase in the efficiency of ZnO after the addition of H_2O_2 is attributed to the availability of more reactive hydroxyl radicals that further hinder the charge recombination of the charged particles (electrons and holes) [45]. Furthermore, in the cases of Pani/ZnO and AgNPs@Pani/ZnO, the degradation of phenol with the addition of H_2O_2 was measured to be 93.05 and 97.91%, respectively, under the same experimental conditions. In summary, active radical sites can be produced by adding H_2O_2, which eventually enhances the degradation phenomenon through oxidation [46].

Role of catalyst dosage for phenol degradation. Catalyst dosage is also a crucial factor to enhance or decrease photocatalytic efficiency. Therefore, knowledge of the optimal amount of photocatalyst is essential to obtain the maximum degradation of the pollutants. Light scattering and screening effects may reduce the degradation efficiency once the catalyst dosage exceeds the optimal value [47]. Therefore, a series of experiments were conducted to determine the optimal dosage of AgNPs@Pani/ZnO for the max-

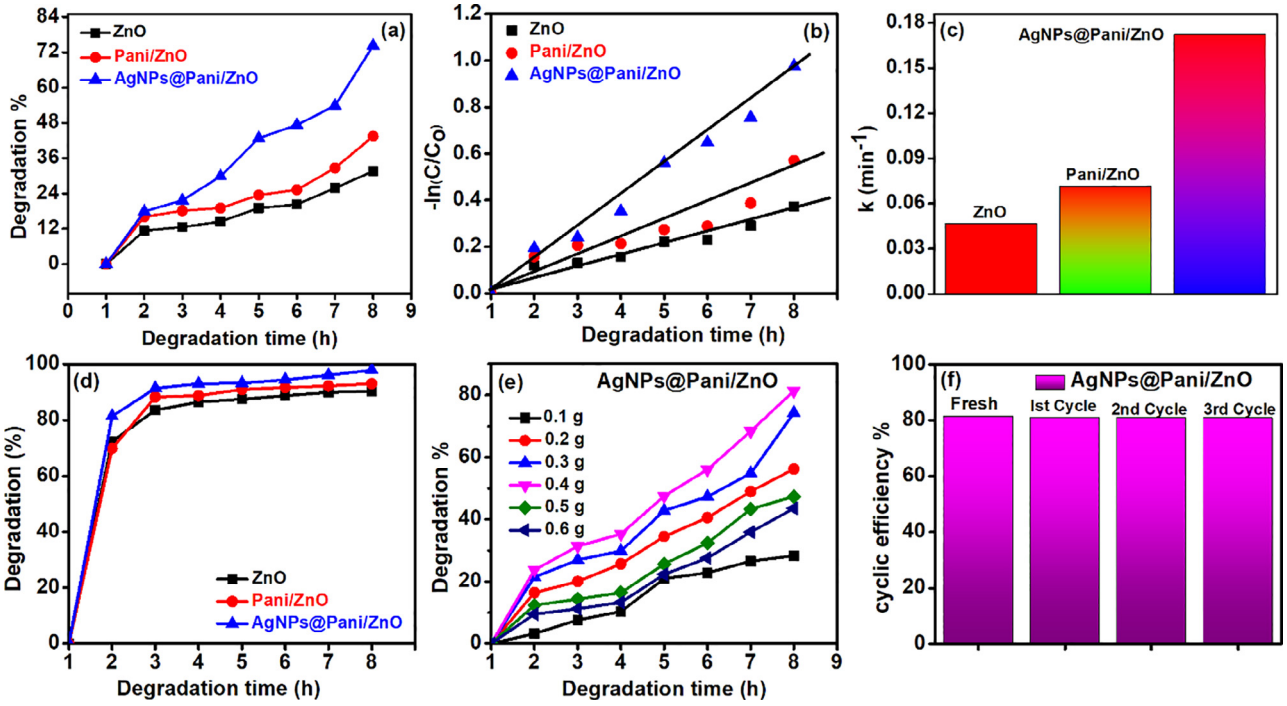

Fig. 9. (a) Degradation percentage, (b) calculated kinetic rate, (c) apparent rate constant, (d) effect of H_2O_2 for ZnO, Pani/ZnO, and AgNPs@Pani/ZnO, (e) effect of the catalyst dosage for AgNPs@Pani/ZnO and (f) reusability of AgNPs@Pani/ZnO for four consecutive cycles.

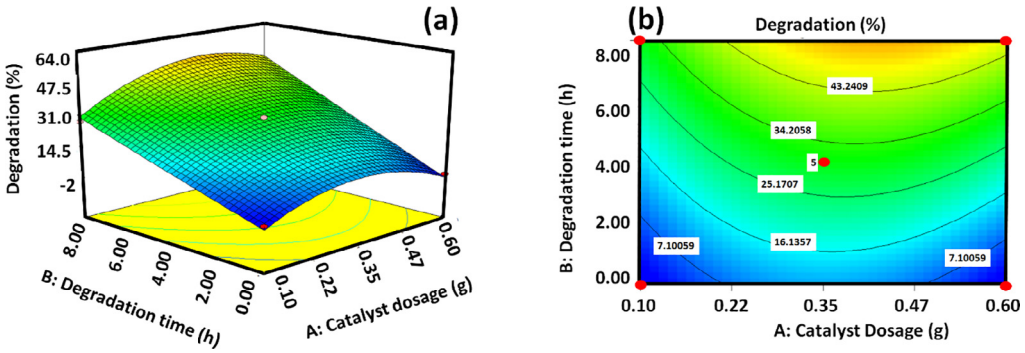

Fig. 10. Three-dimensional (a) and two-dimensional contour RSM graphs for optimized catalyst dosage for AgNPs@Pani/ZnO (b).

imum phenol degradation. The catalyst dosage was varied from 0.1 to 0.6 g with an interval of 0.1 g. The catalytic activity of AgNPs@Pani/ZnO (Fig. 9e) was found to increase with increased dosage from 0.1 g to 0.4 g and was 81.39%. However, at dosages of the catalyst over 0.4 g, the efficiency declined. Consequently, 0.5 and 0.6 g doses of catalyst showed a decreasing trend in the efficiency of AgNPs@Pani/ZnO. Therefore, 0.4 g was the optimal catalyst dosage, with maximum degradation efficiency compared to 0.1 g, 0.2, 0.3, 0.5, and 0.6 g. These results also indicated the light-shielding effect at higher dosages, that is, at 0.5 and 0.6 g. Moreover, the optimized 0.4 g concentration was used to check the cyclic reusability of AgNPs@Pani/ZnO for four consecutive cycles (Fig. 9d). The catalytic efficiency remained remained to be 80.75% after the fourth cycle. These results indicated the potential usage of AgNPs@Pani/ZnO for phenol degradation under visible light. The pH of the reaction is also one the major factors which effect the photocatalytic efficiency. The surface charge, size and morphology of the subjected photocatalyst is affected by the change in pH which ultimately affects the reaction efficiency [48]. The degradation efficiency of AgNPs@Pani/ZnO investigated at different pH of 3, 5, 7, 9 and 11 showed increase in the photocatalytic phenol degradation with the rise in pH from 3 to 9 and afterwards the degradation efficiency decreased on further increase in pH to 11 (Supplementary Fig. S4). The enhanced photocatalytic efficiency in alkaline pH is attributed to the release of more hydroxyl groups [49] which ultimately enhanced the photocatalytic efficiency of AgNPs@Pani/ZnO.

Response surface methodology

In addition to catalyst dosage optimization, Design-Expert software was also used to predict the degradation efficiency of AgNPs@Pani/ZnO. For this purpose, the catalyst dosage was chosen as the variable (0–0.6 g) concerning irradiation time. A total of 13 experiments was run randomly to predict the degradation of phenol. This random test run reduced the systematic bias caused by the catalyst dosage to the irradiation time. The following equation was obtained to predict the phenol degradation by changing the catalyst dosage and irradiation time of AgNPs@Pani/ZnO under the set experimental conditions.

$$\begin{aligned} Degradation = {} & (-14.06289) + (141.4058 * Catalystdosage) \\ & + (3.56996 * Irradiationtime) \\ & + (3.80636 * Catalystdosage * Irradiationtime) \\ & - (201.21756 * Catalystdosage^2) + (.016952 \\ & * Irradiationtime^2 \end{aligned}$$

Moreover, the detail of each designed experiment and their relevant degradation of phenol is documented in Table S3 (Supplementary Information). Furthermore, the ANOVA model was applied to check and test the designed hypotheses for phenol degradation using AgNPs@Pani/ZnO. The results are documented in Table 1, and the F-value was around 159.99, which indicated that the model is significant with a chance of 0.01%.

Photocatalytic hydrogen production

A catalyst dosage of 0.4 g resulted in the maximum phenol degradation; therefore, this dosage was used for the hydrogen production experiment. The hydrogen production of ZnO was (Fig. 11a) 985.3 μmol $g^{-1,}$ and this low hydrogen production is attributed to the high charge recombination ratio and short exciton diffusion of semiconductors with a wide bandgap [50]. However, Pani/ZnO had hydrogen production of 1702.1 μmol g^{-1}, i.e. 1.72 times higher than ZnO. This enhancement is attributed to the π-π* transition, which reduces the bandgap, lowers the charge recombination ratio, and increases the charge carrier mobility [51]. The hydrogen production was further increased by adding Ag and was around 1.58 and 2.74 times higher than that of Pani/ZnO and ZnO, respectively. These results indicate the positive role of Ag in enhancing hydrogen production. The SPR of Ag helped in delaying the recombination ratio while increasing the formation ratio of the charge carriers, thereby reducing the bandgap [52], as confirmed by optical observations shown in Fig. 7. Fig. 11b

Table 1
ANOVA model through RSM for AgNPs@Pani/ZnO.

Source	Sum of Squares	df	Mean Square	F-Value	p-value Prob > F	
Model	4557.104646	5	911.4209291	159.9937	< 0.0001	significant
A-Catalyst dosage	124.4889807	1	124.4889807	21.85319	0.0023	
B-Irradiation time	3248.570582	1	3248.570582	570.2643	< 0.0001	
AB	57.95365805	1	57.95365805	10.17337	0.0153	
A^2	1100.231154	1	1100.231154	193.138	< 0.0001	
B^2	0.511752047	1	0.511752047	0.089835	0.7731	
Residual	39.87623506	7	5.696605008			
Lack of Fit	39.87623506	3	13.29207835			

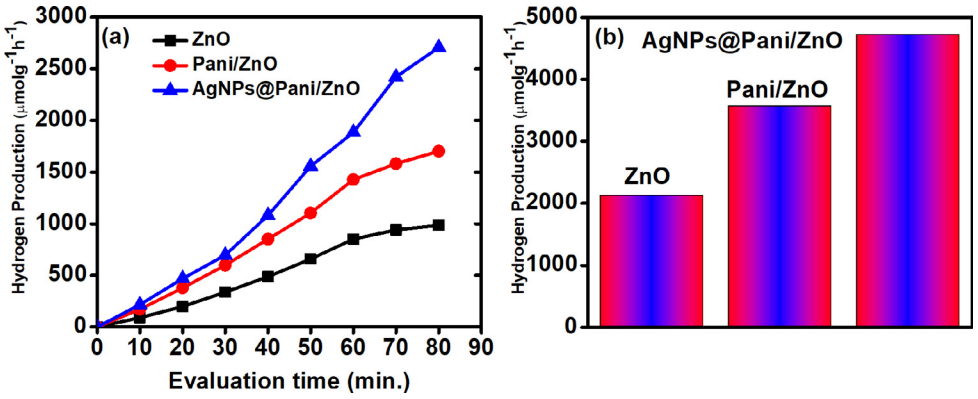

Fig. 11. (a) Hydrogen production and (b) reaction rate of ZnO, Pani/ZnO, and AgNPs@Pani/ZnO,

shows the hydrogen production rates for ZnO, Pani/ZnO, and AgNPs@Pani/ZnO.

The rate of hydrogen production can be adjusted by adjusting the pH of the reaction media. The charge on the catalyst is pH dependent and thus the change in pH may alter the valence and conduction bands level during the redox reaction [53,54]. The AgNPs@Pani/ZnO shows (supplementary Fig. S5) the change in hydrogen production with the change in pH which ranged from 3371.81 to 4713.09 μmol g^{-1} at 3 and 9 pH respectively. Thus, it can be concluded that the volume of produced hydrogen can be easily controlled by adjusting the reaction pH [53].

Proposed photocatalytic mechanism

The proposed mechanism for the degradation of phenol by AgNPs@Pani/ZnO is shown in Fig. 12. There seems three different possibilities for the formation of binary and ternary heterojunctions with ZnO. Considering the binary heterojunction of ZnO

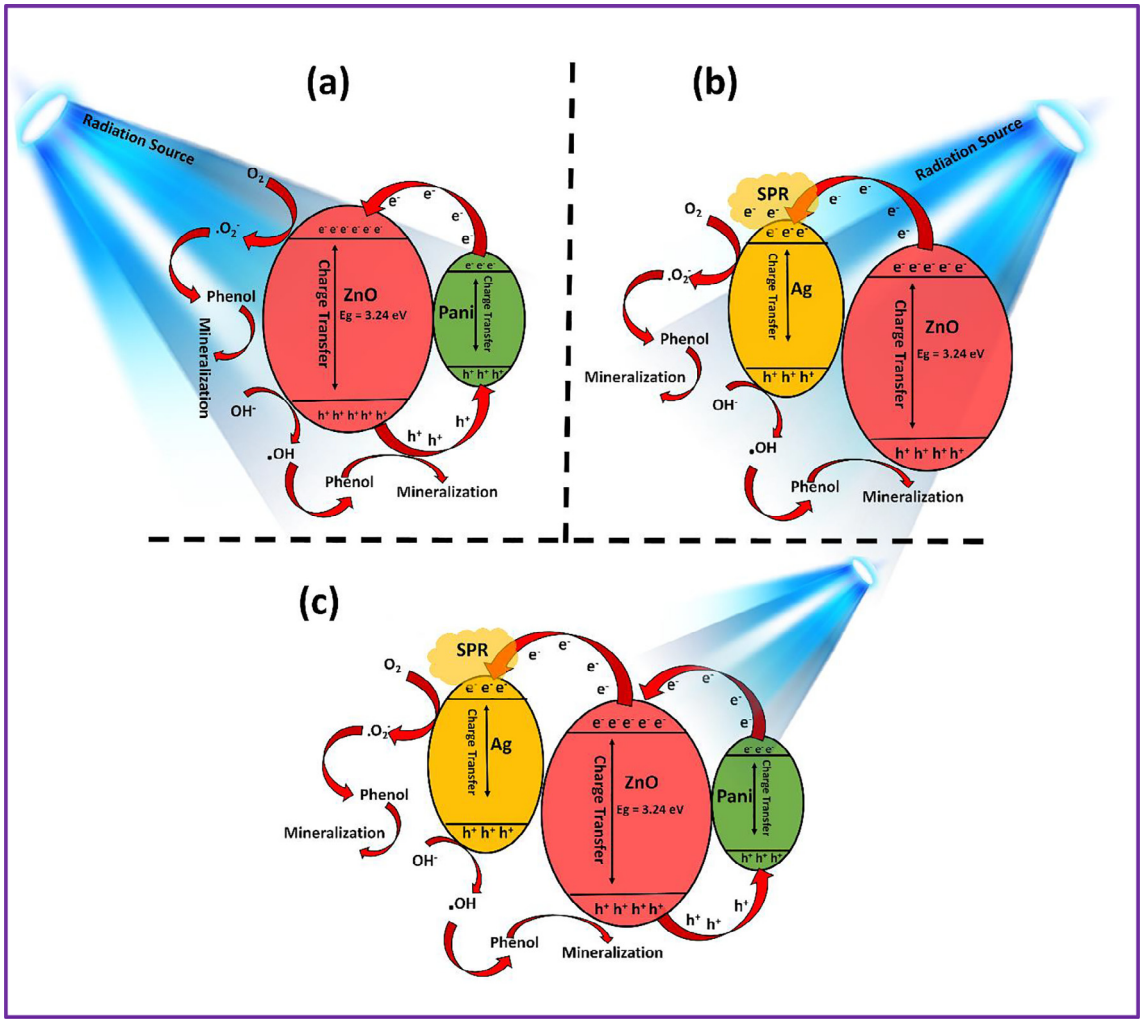

Fig. 12. Proposed photocatalytic mechanisms: (a-b) the formation of possible binary heterojunctions and (c) ternary heterojunctions of AgNPs@Pani/ZnO.

and Pani (Fig. 12a), the energy level of the highest occupied molecular orbital for Pani is between the CB and VB of ZnO. Upon the irradiation of Pani/ZnO with visible light, ZnO transfers the holes to Pani, and consequently, the electrons are transported to the conduction band of ZnO. Furthermore, the excess holes in Pani reacts with the phenol, and oxidation results in the degradation of phenol. Moreover, the generated electron reacts with the dissolved oxygen, contributing to the degradation of the phenol. In the case of an Ag@ZnO binary heterojunction (Fig. 12b), the difference in the work functions of ZnO (5.2 eV) and Ag (4.26 eV) leads to the transport of electrons from ZnO to the CB of the Ag [55]. This indicates the role of Ag as electron storage, which further reduces the charge recombination ratio by producing the Schottky barrier and enhances the photocatalytic degradation under visible light [56]. In addition to these factors, the SPR of Ag also promotes electron movement by harvesting photons, thus helping in the enhancement of photocatalytic activity. For the formation of ternary heterojunctions in AgNPs@Pani/ZnO (Fig. 12c), it can be hypothesized that holes move to Pani, which transfers electrons to the conduction band of ZnO, and ZnO will eventually transfer electrons to the conduction band of Ag, where they accelerate the oxidation and reduction processes to produce free radicals. These radicals are captured by the phenol, resulting in the degradation process. However, several other factors also affect the photocatalytic degradation process, such as grain size, morphology, and chemical state interactions of the photocatalyst.

XPS analysis showed increase in oxygen vacancies, which provided attractive sites to capture the phenolic compounds during the degradation process. Moreover, the interaction bonding of O=C–N and C–O and the SPR of Ag enhanced the efficiency of AgNPs@Pani/ZnO for phenol degradation.

Conclusion

In this research, the hydrogen production and the photocatalytic activity of AgNPs@Pani/ZnO were successfully compared with those of Pani/ZnO and ZnO. Structural, surface chemical state, and optical conduction were investigated to understand the enhanced phenol degradation and hydrogen production with AgNPs@Pani/ZnO. The Ag and Pani affected the movement of the charge carrier by reducing the bandgap from 3.24 eV to 3.13 eV. XPS analysis revealed the potential of C–C, C–O, C–N, O–C=O, and $-N^{+}$ functional groups to contribute to the phenol degradation and hydrogen production process. Diffraction analysis confirmed the variation in grain size without changing the preferred crystal orientation. More interestingly, environmental features such as catalyst dosage, irradiation time, and pH affect the rate of phenol degradation by AgNPs@Pani/ZnO.

The RSM was used to design and predict phenol degradation equations by varying the experimental conditions and ANOVA results were found to be statistically significant. Finally, a proposed mechanism for the degradation of phenol through AgNPs@Pani/ZnO involves the transfer of holes from ZnO to Pani, eventually causing the electrons to transfer from Pani to ZnO and finally toAg from the ZnO with supporting SPR. This mechanism accelerates the oxidation and reduction processes to produce free radicals, which are desirable for the enhanced degradation of phenol. Based on this study, the use of metals and polymers over metal oxides can remediate environmental issues in an easy and precise way.

Declaration of Competing Interest

The authors declare that they have no known competing financial interests or personal relationships that could have appeared to influence the work reported in this paper.

Acknowledgement

This project was funded by the Deanship of Scientific Research (DSR), King Abdulaziz University, Jeddah, Saudi Arabia under grant no. (KEP-1-194-40). The authors, therefore, acknowledge with thanks DSR technical and financial support.

Appendix A. Supplementary data

Supplementary data to this article can be found online at https://doi.org/10.1016/j.jiec.2022.02.021.

References

[1] Z. Taherian, A. Khataee, N. Han, Y. Orooji, J. Ind. Eng. Chem. (2021).
[2] C.H. Lee, B.W. Kwon, J.H. Oh, S. Kim, J. Han, S.W. Nam, S.P. Yoon, K.B. Lee, H.C. Ham, J. Ind. Eng. Chem. 105 (2022) 563–570.
[3] X. Wang, Z. Jin, J. Ind. Eng. Chem. 103 (2021) 222–231.
[4] Y.-H. Song, S. Hidayat, A.J. Effendi, J.-Y. Park, J. Ind. Eng. Chem. 94 (2021) 302–308.
[5] Y.H. Jia, J.H. Ryu, C.H. Kim, W.K. Lee, T.V.T. Tran, H.L. Lee, R.H. Zhang, D.H. Ahn, J. Ind. Eng. Chem. 18 (2012) 715–719.
[6] E. Panisko, T. Wietsma, T. Lemmon, K. Albrecht, D. Howe, Biomass Bioenergy 74 (2015) 162–171.
[7] L.G.C. Villegas, N. Mashhadi, M. Chen, D. Mukherjee, K.E. Taylor, N. Biswas, Curr. Pollut. Rep. 2 (2016) 157–167.
[8] I. Tews, A. Garcia, M. Ayiania, S.H. Mood, K. Mainali, J.-S. McEwen, M. Garcia-Perez, Biomass Convers. Biorefin. (2021) 1–15.
[9] D. Hank, Z. Azi, S.A. Hocine, O. Chaalal, A. Hellal, J. Ind. Eng. Chem. 20 (2014) 2256–2263.
[10] T.A. Saleh, A.M. Elsharif, S. Asiri, A.-R.-I. Mohammed, H. Dafalla, Environ. Nanotechnol. Monit. Manage. 14 (2020) 100302.
[11] J. Guo, C. Wu, J. Zhang, X. Qi, S. Lv, S. Jiang, T. Zhou, D. Lu, C. Feng, X. Chang, Environ. Int. 139 (2020) 105692.
[12] Z. Wang, S. Li, S. Ge, S. Lin, J. Agric. Food. Chem. 68 (2020) 3330–3343.
[13] ATSDR, (2018).
[14] M. Rani, U. Shanker, Colloids Surf., A 553 (2018) 546–561.
[15] A. Saravanan, P.S. Kumar, D.-V.-N. Vo, P.R. Yaashikaa, S. Karishma, S. Jeevanantham, B. Gayathri, V.D. Bharathi, Environ. Chem. Lett. (2020) 1–23.
[16] A. Jilani, G.U. Rehman, M.O. Ansari, M.H.D. Othman, S.Z. Hussain, M.R. Dustgeer, R. Darwesh, New J. Chem. 44 (2020) 19570–19580.
[17] A. Yadav, H. Kumar, R. Sharma, R. Kumari, Colloid Interface Sci. Commun. 40 (2021) 100339.
[18] M.O. Ansari, M.M. Khan, S.A. Ansari, J. Lee, M.H. Cho, RSC Adv. 4 (2014) 23713–23719.
[19] A. Jilani, S.Z. Hussain, M.O. Ansari, R. Kumar, M.R. Dustgeer, M.H.D. Othman, M. Barakat, A.A. Melaibari, J. Mater. Sci. 56 (2021) 7434–7450.
[20] H. Wang, S. Cao, B. Yang, H. Li, M. Wang, X. Hu, K. Sun, Z. Zang, Solar RRL 4 (2020) 1900363.
[21] Y.K. Mishra, G. Modi, V. Cretu, V. Postica, O. Lupan, T. Reimer, I. Paulowicz, V. Hrkac, W. Benecke, L. Kienle, ACS Appl. Mater. Interfaces 7 (2015) 14303–14316.
[22] K. Awazu, M. Fujimaki, C. Rockstuhl, J. Tominaga, H. Murakami, Y. Ohki, N. Yoshida, T. Watanabe, J. Am. Chem. Soc. 130 (2008) 1676–1680.
[23] X. Chen, Z. Zheng, X. Ke, E. Jaatinen, T. Xie, D. Wang, C. Guo, J. Zhao, H. Zhu, Green Chem. 12 (2010) 414–419.
[24] M.M. Hossain, M.A. Islam, H. Shima, M. Hasan, M. Hilal, M. Lee, RSC Adv. 8 (2018) 16927–16936.
[25] M.O. Ansari, S.K. Yadav, J.W. Cho, F. Mohammad, Compos. B Eng. 47 (2013) 155–161.
[26] M.R. Dustgeer, S.T. Asma, A. Jilani, K. Raza, S.Z. Hussain, M.B. Shakoor, J. Iqbal, M.S. Abdel-wahab, R. Darwesh, Inorg. Chem. Commun. 128 (2021) 108606.
[27] M.A. Mudassir, S.Z. Hussain, A. Jilani, H. Zhang, T.M. Ansari, I. Hussain, Langmuir 35 (2019) 8996–9003.
[28] A. Mehto, V. Mehto, J. Chauhan, I. Singh, R. Pandey, J. Nanomed. Res. 5 (2017) 1–8.
[29] N. Turkten, Y. Karatas, M. Bekbolet, Water 13 (2021) 1025.
[30] A. Jilani, M.H.D. Othman, M.O. Ansari, I. Ullah Khan, S.Z. Hussain, Synth. Met. 251 (2019) 30–39.
[31] F. Ahmed, S. Kumar, N. Arshi, M.S. Anwar, L. Su-Yeon, G.-S. Kil, D.-W. Park, B.H. Koo, C.G. Lee, Thin Solid Films 519 (2011) 8375–8378.
[32] R. Singh, P.B. Barman, D. Sharma, J. Mater. Sci.: Mater. Electron. 28 (2017) 5705–5717.
[33] N. Sharma, J. Kumar, S. Thakur, S. Sharma, V. Shrivastava, Drug Invent. Today 5 (2013) 50–54.
[34] J.F. Moulder, Phys. Electron. (1995) 230–232.
[35] C. Wang, D. Wu, P. Wang, Y. Ao, J. Hou, J. Qian, Appl. Surf. Sci. 325 (2015) 112–116.
[36] W. Li, D. Du, T. Yan, D. Kong, J. You, D. Li, J. Colloid Interface Sci. 444 (2015) 42–48.

[37] K.N. Wood, S.T. Christensen, D. Nordlund, A.A. Dameron, C. Ngo, H. Dinh, T. Gennett, R. O'Hayre, S. Pylypenko, Surf. Interface Anal. 48 (2016) 283–292.
[38] M.A. Domínguez-Crespo, A.B. López-Oyama, A.M. Torres-Huerta, A.R. Hernández-Basilio, D. Palma-Ramírez, J.A. Lois-Correa, D.S. García-Zaleta, J. Nanomater. 2019 (2019) 2872460.
[39] J.Y. Tai, K.H. Leong, P. Saravanan, L.C. Sim, Bioinspired Synthesis of Carbon Dots/g-C3N4 Nanocomposites for Photocatalytic Application, EDP Sciences, 2018, p. 05015.
[40] N. Kamarulzaman, M.F. Kasim, R. Rusdi, Nanoscale Res. Lett., 10 (2015) 1034-1034.
[41] J. Liqiang, Q. Yichun, W. Baiqi, L. Shudan, J. Baojiang, Y. Libin, F. Wei, F. Honggang, S. Jiazhong, Sol. Energy Mater. Sol. Cells 90 (2006) 1773–1787.
[42] R. Bhaskar, A. Lakshmanan, S. Marimuthu, T. Ravishankar, M.T. Jose, L. Nariangadu, Indian J. Pure Appl. Phys. 47 (2009) 772–774.
[43] G. Reddy, J. Reddy, R.H. Krishna, G. Gopal, J. Asian Ceram. Soc. 5 (2017).
[44] X. Zhang, Z. Zhao, W. Zhang, G. Zhang, D. Qu, X. Miao, S. Sun, Z. Sun, Small 12 (2016) 793–801.
[45] D. Saha, M.M. Desipio, T.J. Hoinkis, E.J. Smeltz, R. Thorpe, D.K. Hensley, S.G. Fischer-Drowos, J. Chen, J. Environ. Chem. Eng. 6 (2018) 4927–4936.
[46] L. Shen, N. Bao, Y. Zheng, A. Gupta, T. An, K. Yanagisawa, J. Phys. Chem. C 112 (2008) 8809–8818.
[47] N.N. Yunus, F. Hamzah, M.S. So'aib, J. Krishnan, IOP Conf. Series: Mater. Sci. Eng. 206 (2017) 012092.
[48] A. Kumar, G. Pandey, Mater. Sci. Eng. Int. J 1 (2017) 1–10.
[49] F. Habtamu, S. Berhanu, T. Mender, J. Chem. 2021 (2021).
[50] D.B. Ingram, S. Linic, J. Am. Chem. Soc. 133 (2011) 5202–5205.
[51] M.S. Hamdy, H.S.M. Abd-Rabboh, M. Benaissa, M.G. Al-Metwaly, A.H. Galal, M. A. Ahmed, Opt. Mater. 117 (2021) 111198.
[52] J. Jiao, J. Wan, Y. Ma, Y. Wang, RSC Adv. 6 (2016) 106031–106034.
[53] B. Huang, R.R. Rao, S. You, K. Hpone Myint, Y. Song, Y. Wang, W. Ding, L. Giordano, Y. Zhang, T. Wang, S. Muy, Y. Katayama, J.C. Grossman, A.P. Willard, K. Xu, Y. Jiang, Y. Shao-Horn, JACS Au, 1 (2021) 1674-1687.
[54] Y. Shen, Y. Zhan, S. Li, F. Ning, Y. Du, Y. Huang, T. He, X. Zhou, Chem. Sci. 8 (2017) 7498–7504.
[55] Z. Wang, X. Ye, L. Chen, P. Huang, Q. Wang, L. Ma, N. Hua, X. Liu, X. Xiao, S. Chen, Mater. Sci. Semicond. Process. 121 (2021) 105354.
[56] M. Sabzehparvar, F. Kiani, N.S. Tabrizi, J. Alloy. Compd. 876 (2021) 160133.